

# Electron-phonon properties and superconductivity of doped antimonene

A. V. Lugovskoi,<sup>1,\*</sup> M. I. Katsnelson,<sup>1,2</sup> and A. N. Rudenko<sup>3,1,2</sup>

<sup>1</sup>*Institute for Molecules and Materials, Radboud University, Heijendaalseweg 135, NL-6525 AJ Nijmegen, The Netherlands*

<sup>2</sup>*Theoretical Physics and Applied Mathematics Department, Ural Federal University, 620002 Ekaterinburg, Russia*

<sup>3</sup>*School of Physics and Technology, Wuhan University, Wuhan 430072, China*

Antimonene is a recently discovered two-dimensional semiconductor with exceptional environmental stability, high carrier mobility, and strong spin-orbit interactions. In combination with electric field, the latter provides an additional degree of control over the materials' properties because of induced spin splitting. Here, we report on a computational study of electron-phonon coupling and superconductivity in *n*- and *p*-doped antimonene, where we pay a special attention on the effect of the perpendicular electric field. We find that at realistic carrier concentrations, antimonene can be turned into a state with strong electron-phonon coupling, with the mass enhancement factor  $\lambda$  of up to five. In this regime, antimonene is expected to be a superconductor with the critical temperature of  $\sim 17$  K. Application of bias voltage leads to a considerable modification of the electronic structure, affecting the electron-phonon coupling in antimonene. While these effects are less obvious in case of electron-doping, field-effect in hole-doped antimonene results in a considerable variation of the critical temperature depending on bias voltage.

## I. INTRODUCTION

Antimonene is a recent addition [1, 2] to a growing family of elemental two-dimensional (2D) materials. This monolayer phase of antimony adopts buckled honeycomb lattice ( $D_{3d}$  point group), similar to those of silicene [3] and germanene [4], or more recently discovered blue phosphorene [5]. Antimonene was successfully obtained by various experimental techniques [6], including, but not limited to, epitaxial growth [7], liquid and solid phase exfoliation [8, 9]. Based on both experimental observation and *ab initio* modeling [1, 9], antimonene is believed to be a material with remarkable stability on air and in water [7, 9]. This alone makes antimonene an appealing candidate for various applications because instability at realistic conditions is one of the main factors limiting the application of 2D materials [10, 11]. From the fundamental point of view, characteristic feature of antimonene is a strong spin-orbit coupling (SOC) [12], with the intraatomic SOC constant  $\lambda_{\text{SOC}} = 0.34$  eV. Proper account of SOC is important for a correct description of the electronic structure and effective masses [12]. Antimonene is expected to have high carrier mobility [13] comparable or exceeding that of the other 2D semiconductors. Besides, monolayer Sb is an indirect band semiconductor with a theoretically estimated band gap of 1.2 eV [14]. These properties make antimonene suitable for application in electronic [13] and optical devices [14], where thickness- and strain-tunable band gap could provide an additional control over the material's properties [1, 15].

Superconductivity is not uncommon for two-dimensional materials [16]. It is observed in thin films [17], atomic sheets [18], surface atomic layers [19] and other 2D structures of various chemical composition. Recent experimental works [18, 20] revealed

superconductivity in graphene laminates with the critical temperatures  $T_c$  in the range of 4–6 K. Magnetization measurements of intercalated black phosphorus reveal  $T_c = 3.8 \pm 0.1$  K, which is independent of the intercalation type [21]. Also, a large number of experimental measurements of  $T_c$  were recently performed for doped 2D transition metal dichalcogenides:  $\text{WS}_2$  and  $\text{NbSe}_2$  were demonstrated to be superconducting below 3 K [22, 23], while  $\text{MoS}_2$  was reported to have  $T_c$  in the range of 7–11 K [24, 25]. Superconductivity in two dimensions is especially interesting in view of the possibility to control the electronic structure of 2D materials by strain, electric field, thickness, or substrate. Superconducting 2D materials also appear as an appealing testbed for studying interface phenomena and proximity effects. In particular, 2D materials can be implemented as a part of the Josephson junction [26, 27].

Computational studies predicting the superconductivity in monolayer graphene [28, 29] and phosphorene [30] were preceding the experimental observations [18, 20, 21]. Also, superconductivity at nonzero charge doping has already been predicted for recently proposed arsenene [31] (monolayer As), as well as for silicene [32]. Experimental data on superconductivity of these materials are not available yet. While theoretical studies lack realistic account of the experimental setup, they allow to study underlying mechanisms of superconductivity, for example, the key contributions to electron-phonon coupling or important changes of electronic structure due to carrier doping [33]. Additionally, there is an opportunity to study modifications of the electronic structure and electron-phonon coupling properties including  $T_c$  in the presence of strain [30] or other external factors. Neither calculations nor measurements of  $T_c$  are available in the literature for doped antimonene.

In this paper, we present a systematic study of the electron-phonon coupling and conventional superconductivity in *n*- and *p*-doped antimonene. To this end, we use a combination of Density Functional Theory

\* [alugovskoi@science.ru.nl](mailto:alugovskoi@science.ru.nl)

(DFT) [34, 35] and Density Functional Perturbation Theory (DFPT) [36] in conjunctions with the formalism of Maximally Localized Wannier Functions (MLWF) [37, 38]. Besides charge doping, we also consider the role of electric field applied in the direction perpendicular to atomic layer, which allows to modify the band structure. Considering the interplay of these effects is interesting for a number of reasons. For example, perpendicular electric field allows to control the band gap and effective masses in a silicene and germanene [39, 40], as well as in few-layer phosphorene [41–43], where it is possible to transform material from normal insulator to topological insulator or metal. Besides this, perpendicular electric field breaks inversion symmetry, which, in combination with strong SOC, induces spin-splitting of both valence and conduction bands [44]. This case is observed, for example, in experimental work [25], where setup combining liquid and solid gating is used to study superconductivity in MoS<sub>2</sub> flakes, and ionic liquid naturally creates the environment for emergence of perpendicular electric field. Since SOC in antimonene is strong, this situation is particularly interesting to study. For these reasons, additionally to carrier doping, we take into account electric field in our calculations and study dependence of the electron-phonon coupling on bias voltage.

The rest of the paper is organized as follows. We first present the theory and computational methods used to calculate the electron-phonon coupling and superconducting critical temperatures, and also discuss the relevant approximations (Sec. II). We then give a description of the calculated electronic structure and phonon dispersion of antimonene (Sec. III A). Main results are presented in Sec. III B, where we discuss the obtained dependencies of  $T_c$  and electron-phonon coupling strength, as well as superconducting transition temperatures on carrier concentrations, with a detailed consideration of the most important cases. The effect of a perpendicular electric field (bias voltage) is analyzed and discussed in Sec. III C. In Sec. IV, we summarize our results and conclude the paper.

## II. THEORETICAL BACKGROUND AND COMPUTATIONAL DETAILS

### A. Electron-phonon coupling and Allen-Dynes-McMillan equation

In this section, we give a short theoretical description of the electron-phonon coupling and its relation to superconductivity. More detailed description of the theory from the viewpoint of *ab initio* calculations can be found in Ref. 45.

The interaction of electrons with phonons is described by the matrix elements

$$g_{mn,\nu}(\mathbf{k}, \mathbf{q}) = \left( \frac{\hbar}{2m_0\omega_{\mathbf{q}\nu}} \right)^{1/2} M_{mn}^{\nu}(\mathbf{k}, \mathbf{q}), \quad (1)$$

where

$$M_{mn}^{\nu}(\mathbf{k}, \mathbf{q}) = \langle \psi_{m\mathbf{k}+\mathbf{q}} | \partial_{\mathbf{q}\nu} V | \psi_{n\mathbf{k}} \rangle, \quad (2)$$

and  $\psi_{n\mathbf{k}}$  is the electronic Bloch function for band  $n$  and wavevector  $\mathbf{k}$ ,  $\partial_{\mathbf{q}\nu} V$  is the derivative of the self-consistent potential associated with the phonon of wavevector  $\mathbf{q}$ , branch index  $\nu$ , and frequency  $\omega_{\mathbf{q}\nu}$ , and  $m_0$  is the atomic mass.

It is useful to define a dimensionless representation of the electron-phonon coupling associated with the single phonon mode  $\nu$  and wavevector  $\mathbf{q}$  as an average over the Fermi surface:

$$\lambda_{\mathbf{q}\nu} = \frac{1}{N_F \omega_{\mathbf{q}\nu}} \sum_{mn,\mathbf{k}} w_{\mathbf{k}} |g_{mn,\nu}(\mathbf{k}, \mathbf{q})|^2 \times \delta(\varepsilon_{n\mathbf{k}} - \varepsilon_F) \delta(\varepsilon_{m\mathbf{k}+\mathbf{q}} - \varepsilon_F), \quad (3)$$

which is closely related to the Eliashberg electron-phonon spectral function  $\alpha^2 F(\omega)$

$$\alpha^2 F(\omega) = \frac{1}{2} \sum_{\mathbf{q}\nu} w_{\mathbf{q}} \omega_{\mathbf{q}\nu} \lambda_{\mathbf{q}\nu} \delta(\omega - \omega_{\mathbf{q}\nu}), \quad (4)$$

where  $w_{\mathbf{k}}$  ( $w_{\mathbf{q}}$ ) is the symmetry-dependent weight of  $\mathbf{k}$  ( $\mathbf{q}$ ) points,  $\varepsilon_{n\mathbf{k}}$  ( $\varepsilon_{m\mathbf{k}+\mathbf{q}}$ ) is the electronic energy, and  $N_F$  is the density of states (DOS) at the Fermi energy,  $\varepsilon_F$ .

Besides  $\lambda_{\mathbf{q},\nu}$ , we also consider the nesting function  $\xi_{\mathbf{q}}$  as defined in [46]:

$$\xi_{\mathbf{q}} = \sum_{mn,\mathbf{k}} w_{\mathbf{k}} \delta(\varepsilon_{n\mathbf{k}} - \varepsilon_F) \delta(\varepsilon_{m\mathbf{k}+\mathbf{q}} - \varepsilon_F). \quad (5)$$

The nesting function is independent of electron-phonon coupling matrix elements, while it is useful to understand the effect of the Fermi surface topology.

The critical temperature of the superconducting transition according to the McMillan equation [47], modified by Allen and Dynes [48] can be estimated as:

$$T_c = \frac{\omega_{\log}}{1.2} \exp \left( - \frac{1.04(1 + \lambda)}{\lambda - \mu_c^*(1 + 0.62\lambda)} \right), \quad (6)$$

which is based on the superconductivity theory of Migdal and Eliashberg [49, 50]. Although derivation of Eq. (6) contains a number of approximations, it is a reasonable starting point for the estimation of  $T_c$ . In Eq. (6),  $\mu_c^*$  is the Morel-Anderson effective Coulomb potential [51],

$$\omega_{\log} = \exp \left[ \frac{2}{\lambda} \int_0^{\omega_{\max}} d\omega \frac{\alpha^2 F(\omega)}{\omega} \log \omega \right] \quad (7)$$

is the logarithmically averaged phonon frequency,

$$\lambda = \sum_{\mathbf{q}\nu} w_{\mathbf{q}} \lambda_{\mathbf{q}\nu} \quad (8)$$

is the total Fermi energy-dependent electron-phonon coupling strength, which is also known as the mass-enhancement factor [52]. In the present paper,  $\mu_c^*$  is considered as a phenomenological parameter with the typical values in the range of 0.1–0.2 [45, 47, 48]. The values of  $T_c$ , discussed in text, are obtained with  $\mu_c^* = 0.1$ . Among 2D materials the Coulomb pseudopotential was estimated more rigorously for graphene in Ref. 29 ( $\mu_c^* = 0.16$ ) and Ref. 28 ( $\mu_c^* = 0.1$ ). We note that an accurate estimate of  $\mu_c^*$  requires an account of dielectric screening, and, therefore, would be strongly influenced by the underlying substrate.

## B. Calculation details

The initial electronic structure and crystal structure optimization calculations were performed at the DFT level as implemented in the plane-wave QUANTUM ESPRESSO (QE) code [53, 54], using fully relativistic norm conserving pseudopotentials. Exchange and correlation were treated with the local density approximation (LDA). The kinetic energy cutoff for plane waves was set to 90 Ry, the Brillouin zone was sampled with a (16×16) Monkhorst-Pack k-point mesh [55], and the electronic state occupancies were treated as fixed. The crystal structure was fully relaxed with a threshold of  $1 \times 10^{-12}$  eV for total energies and  $1 \times 10^{-12}$  eV/Å for forces. The vacuum thickness of 30 Å was used to avoid spurious interactions between the supercell periodic images in the direction perpendicular to the 2D plane. The Brillouin zone for phonons within DFPT was sampled by a (16×16) q-point mesh, and the self-consistency threshold of  $1 \times 10^{-16}$  eV was used.

Electronic structure, dynamical matrices and electron-phonon matrix elements obtained from DFT and DFPT calculations were used as the initial data for Wannier interpolation within the MLWF formalism, as implemented in EPW [37, 56]. The calculation of the electron-phonon-related properties was performed on dense grids of (432×432) k- and (208×208) q-points, which ensures the numerical convergence of the results presented in this work.

## C. Role of charge doping, out-of-plane acoustic phonons, and bias voltage

In this work, we simulate the carrier doping of antimonene using the rigid band shift approximation, that leaves the electronic structure and phonon dispersion unchanged. Typically, charge doping in 2D materials mainly affects the out-of-plane mode and optical phonons [29–31]. At the same time, out-of-plane acoustic mode (ZA) is not taken into account in our calculations. Although consideration of ZA mode may be important for fundamental understanding of the associated effects, it is of little practical interest for the superconductiv-

ity studies: interaction of 2D materials with a substrate would suppress out-of-plane vibrations making already small coupling of electrons with these modes negligible. Furthermore, a correct description of such effects is not trivial within the slab geometry. An accurate description of electrons coupling with out-of-plane phonon modes is presented in [57] for doped graphene, where it is also shown, that the contribution from ZA mode is negligible. Optical phonons, as we show below, have a minor effect on the electron-phonon coupling and  $T_c$ . Therefore, the rigid band shift approximation is justified for the purpose of our study. The carrier concentration  $\delta\rho$  is thus chosen in accordance with the ground state DOS and the Fermi energy,  $\delta\rho(\varepsilon_F) = \int_0^{\varepsilon_F} d\varepsilon \rho(\varepsilon)$ .

We consider both *n*- and *p*-doping cases. We limit ourselves to the concentrations less than  $1 \times 10^{15}$  cm<sup>-2</sup>. Although such carrier concentrations correspond to a heavy doping regime, they are not unrealistic. Electron concentrations of the order of  $1 \times 10^{15}$  cm<sup>-2</sup> are achievable in thin metallic films by means of electrochemical techniques [58]. Smaller electron and hole concentrations of the order of  $1 \times 10^{14}$  cm<sup>-2</sup> can be achieved by liquid gating [59] and by solid-electrolyte gating [60].

To simulate the effect of a perpendicular electric field, we consider a tight-binding Hamiltonian obtained in the MLWF basis, and add position-dependent bias voltage, yielding the following Hamiltonian

$$H = \sum_{ij} t_{ij} c_i^\dagger c_j + V_b/d \sum_i z_i c_i^\dagger c_i, \quad (9)$$

where the sum runs over the real-space MLWF orbitals *i* and *j*,  $c_i^\dagger, c_i$  ( $c_j$ ) are the creation and annihilation operators of electrons on the corresponding orbitals,  $z_i$  is the *z*-component of the position operator of the orbital *i*,  $t_{ij}$  is the corresponding hopping integral, *d* is the buckling constant, and *V* is bias voltage applied to the upper and lower planes of antimonene.

## III. RESULTS AND DISCUSSION

### A. Electronic structure and phonon dispersion

We find the calculated relaxed lattice parameter of free-standing antimonene to be 4.0 Å with the buckling constant 1.6 Å, which is consistent with previously reported data [61]. The corresponding electronic band structure is given in Fig. 1(a), from which one can see that antimonene is an indirect gap semiconductor with the gap with of 0.7 eV. The obtained value is less than 1.0 eV and 1.2 eV obtained in Refs. 12 and 14, due to the differences in exchange-correlation functional, but agrees well with the value reported in Ref. 61. The band structure and DOS [Fig. 1(b)] display high degree of electron-hole asymmetry even at small Fermi energies, unlike those of typical 2D materials including graphene and phosphorene.

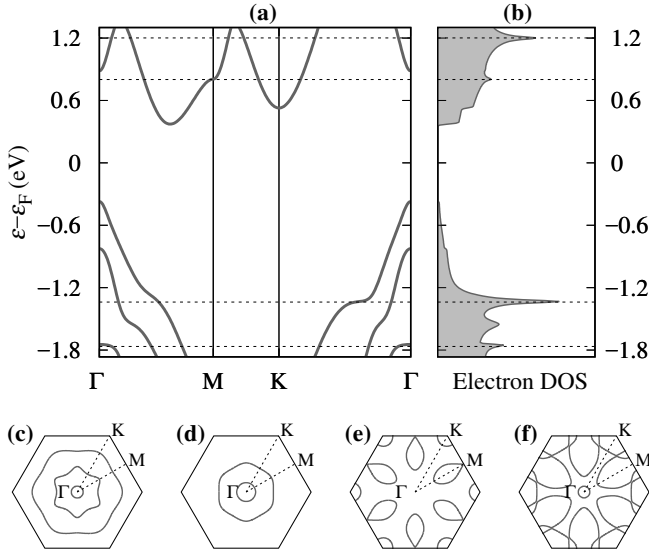


FIG. 1. Electronic structure of antimonene. (a) Band structure plotted along high-symmetry directions of the Brillouin zone. (b) DOS in the relevant carrier concentration range. Horizontal lines on (a) and (b) mark the following carrier concentrations (from bottom to top):  $N_h = 1 \times 10^{15} \text{ cm}^{-2}$ ,  $N_h = 3.7 \times 10^{14} \text{ cm}^{-2}$ ,  $N_e = 4 \times 10^{14} \text{ cm}^{-2}$ ,  $N_e = 1 \times 10^{15} \text{ cm}^{-2}$ . The corresponding Fermi surface contours are given on subplots (c)–(f).

At negative Fermi energies (hole doping) the Fermi surface is initially formed by one valence band. As the Fermi energy reduces, second and third occupied bands get involved, forming three concentric pockets [see Fig. 1(c)]. In the K- $\Gamma$  direction of the electronic structure one can see a flat region in the valence band, which gives rise to a van Hove singularity (VHS) in DOS ( $\varepsilon = -1.3 \text{ eV}$  in Fig. 1). The corresponding constant-energy contour is shown in Fig. 1(d), which exhibits a hexagonal warping. This topology opens up a possibility for the scattering between the parallel regions of the surface, known as the Fermi surface nesting [62, 63]. In this case one can expect an increase of the electron-phonon coupling strength at the corresponding carrier concentrations ( $N_h = 3.7 \times 10^{14} \text{ cm}^{-2}$ ). Further reduction of the Fermi energy leads to a widening of the contours accompanied by the bending of the hexagons, suppressing the nesting effect. The topology of the Fermi surface at positive Fermi energies (electron doping) is determined entirely by a single conduction band, yet involving multiple valleys. At small energies the surface is formed by six closed droplet-shaped pockets, originating from the valleys centered along the  $\Gamma$ -M direction. Additional circle-shaped pockets appear as the Fermi energy reaches the valley at the K-point [Fig. 1(e)]. Further increase of the Fermi energy results in a VHS originating from the band bending around the M point. At even higher conduction band fillings there is a distinctive change in the Fermi surface topology. Namely, previously closed pockets become connected, and an additional valley emerges around  $\Gamma$  [circle region in Fig. 1(f)]. Similar

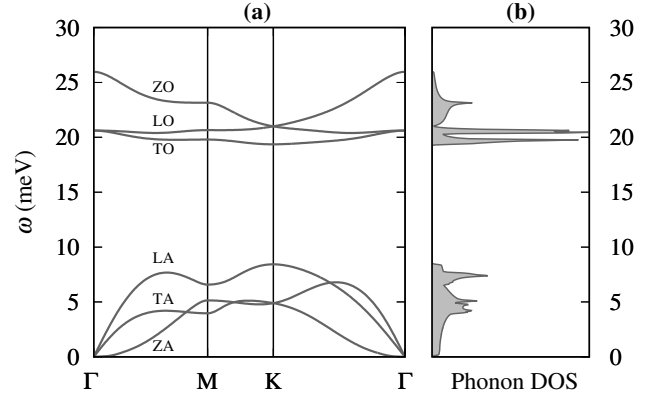


FIG. 2. Phonon spectrum of antimonene. (a) Phonon dispersion plotted along high-symmetry directions of the Brillouin zone. (b) Phonon DOS.

to the valence band, one can see a hexagonal warping around the K point, which gives rise to a VHS ( $\varepsilon = 1.2 \text{ eV}$  in Fig. 1), corresponding to a heavy electron doping with  $N_e = 1.0 \times 10^{15} \text{ cm}^{-2}$ .

Calculated phonon spectra is given on Fig. 2. While the impact of SOC on the electronic structure is notable, it is nearly nonexistent in the context of lattice dynamics: phonon spectra with SOC taken into account only slightly differ from that of without SOC. In comparison to other elemental 2D materials, antimonene has considerably small phonon frequencies, which results, for example, in low thermal conductivity, as seen in [64]. Elastic constants of antimonene, which can be estimated from the frequencies of long-wavelength phonons also have low values. Particularly, independent 2D elastic constants  $C_{11} = 2.1 \text{ eV}/\text{\AA}^2$ , associated with LA phonon mode, and  $C_{66} = 0.8 \text{ eV}/\text{\AA}^2$ , associated with TA phonon mode, while  $C_{12} = C_{11} - 2C_{66} = 0.5 \text{ eV}/\text{\AA}^2$  and Young modulus  $E = (C_{11}^2 - C_{12}^2)/C_{11} = 2.17 \text{ eV}/\text{\AA}^2$ . The corresponding sound velocities are  $v_{s,LA} = 3.4 \text{ km/s}$  and  $v_{s,TA} = 2.1 \text{ km/s}$ . The bending rigidity associated with ZA phonons is  $\kappa = 0.3 \text{ eV}$ . These values are significantly smaller than the elastic moduli and speed of sound of graphene, as well as black and blue phosphorene [65, 66]. Indeed, in contrast to light elements, heavy antimony atoms suppress vibrations, leading to smaller frequencies. Finally, it is interesting to make a note on the role of anharmonic effects in antimonene. The characteristic cutoff wavevector below which anharmonic corrections become dominant is given by  $q^* = \sqrt{\frac{3T_R E}{16\pi\kappa^2}}$ . At room temperature  $T_R = 300 \text{ K}$  it can be estimated as  $q^* = 0.2 \text{ \AA}^{-1}$ , which is order of magnitude larger than for black phosphorus [67] and comparable with graphene [68]. In the context of superconductivity, however, these effects are not relevant.



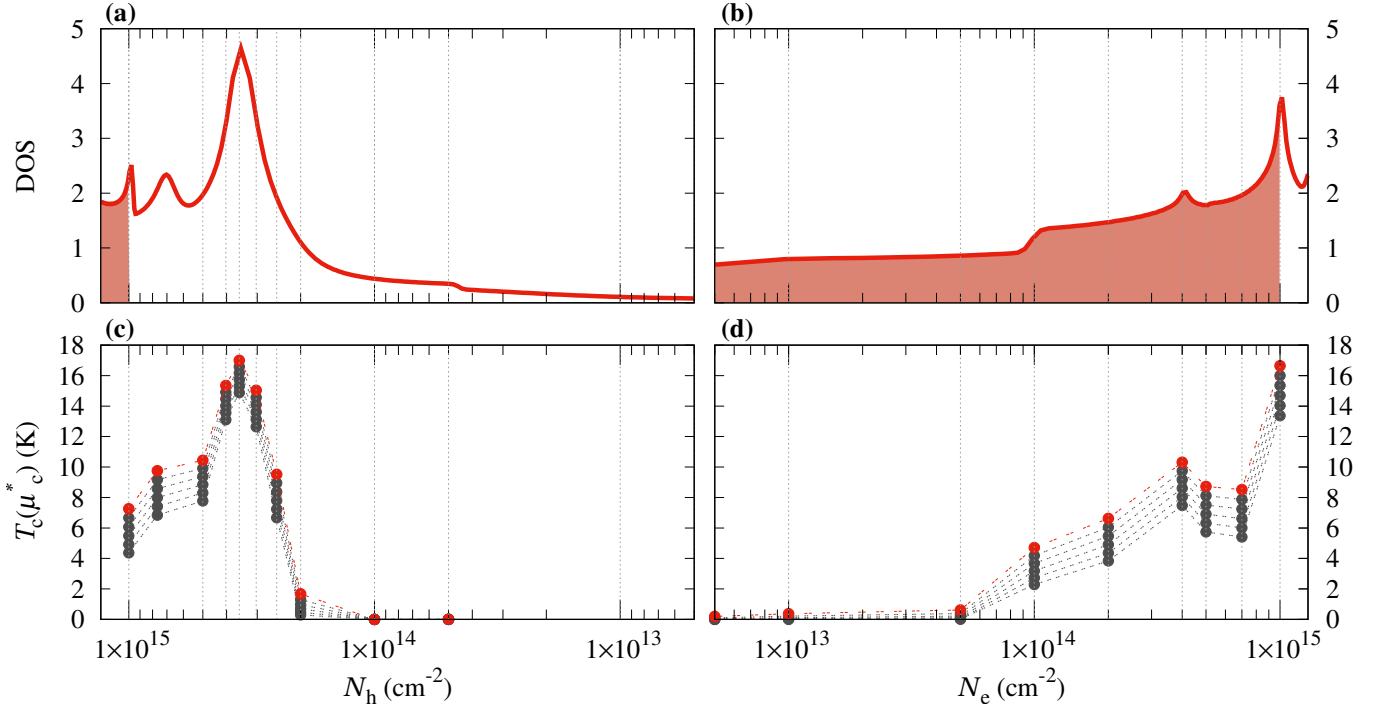


FIG. 3. DOS [(a), (b)] and critical temperature [(c), (d)] dependencies on carrier concentration for antimonene. Vertical dotted lines mark considered carrier concentrations. Multiple points for single  $N_{h/e}$  on (c) and (d) represent  $T_c$  at different values of  $\mu_c^*$  (0.1, 0.12,...0.2) from top to bottom. Red symbols and lines on panels (c) and (d) mark  $T_c$  values at  $\mu_c^* = 0.1$ . Dashed lines on bottom panels serve as a guide to the eye.

### B. Superconductivity and electron-phonon coupling

Calculated values of  $T_c$  at various carrier concentrations are presented in Fig. 3. As can be seen, the concentrations resulting in the highest critical temperature for both holes and electrons correlate with VHS of the corresponding carrier DOS. The highest value  $T_c = 17$  K is achieved for the hole doping with  $N_h = 3.7 \times 10^{14} \text{ cm}^{-2}$ . In the case of electron-doped antimonene, the highest value is comparable ( $T_c \approx 16$  K) yet it is observed at significantly higher carrier concentration  $N_e = 1 \times 10^{15} \text{ cm}^{-2}$ . In all considered cases  $T_c$  decreases by 2–3 K at the maximum chosen  $\mu_c^* = 0.2$ .

For the sake of comparison with experimental results, let us consider reference experimental concentrations reported recently. In the context of superconductivity of intercalated graphene laminates, chemical doping was utilized leading to  $T_c$  in the range 6–6.4 K at  $N_e \approx 1 \times 10^{14} \text{ cm}^{-2}$  [18, 20]. At this concentration antimonene demonstrates slightly lower  $T_c$  right above the liquid helium temperatures (4.2 K). However, carrier concentrations achievable by the electrostatic doping [59, 60, 69] yield higher critical temperatures: 6.6–10.4 K at  $2\text{--}5 \times 10^{14} \text{ cm}^{-2}$  with a local maximum at  $4.1 \times 10^{14} \text{ cm}^{-2}$ . In case of the hole doping,  $T_c$  vanishes rapidly with increasing  $\mu_c^*$  at carrier concentrations below  $2 \times 10^{14} \text{ cm}^{-2}$ , mainly due to small DOS. In the vicinity of VHS  $T_c$  increases rapidly: at

$3 \times 10^{14} \text{ cm}^{-2}$  we find  $T_c = 15.4$  K. This makes the case of hole doping practically interesting. Our estimation for  $T_c$  in antimonene is comparable with that of phosphorene, according to the calculations reported in [19, 30]. At  $N_e = 7 \times 10^{14} \text{ cm}^{-2}$  both materials yield  $T_c \approx 10$  K with phosphorene showing slightly higher values. At smaller concentrations antimonene shows better results: at  $1\text{--}4 \times 10^{14} \text{ cm}^{-2}$  electron-doped phosphorene is predicted to have  $T_c$  in the range of 0.5–5 K, while antimonene exhibits  $T_c = 10$  K. Application of strain to phosphorene can change the situation:  $T_c$  of phosphorene in this case can be tuned to exceed those of monolayer Sb in the aforementioned concentration range [19, 30]. Calculated values of  $T_c$  for the other group V 2D material, namely arsenene, closely resemble those of antimonene, with a slight shift to lower concentrations [31]. Particularly, at concentrations ranging from  $0.9 \times 10^{14}$  till  $3.7 \times 10^{14} \text{ cm}^{-2}$   $n$ -doped arsenene shows  $T_c$  in the range of 4.7–10.1 K, with the maximum value at  $2.8 \times 10^{14} \text{ cm}^{-2}$ , which is just 1 K higher, than for antimonene at the same concentration. As for phosphorene, a strain tuning of  $T_c$  is proposed for arsenene, which can increase these values.

Let us analyze electron-phonon coupling in antimonene and its role in the superconducting properties in more details. Data on the averaged and doping-dependent electron-phonon coupling  $\lambda$  [Eq. (8)] of antimonene is given in Fig. 4 (red triangles). It is worth mentioning that electron-phonon coupling strength of doped-antimonene

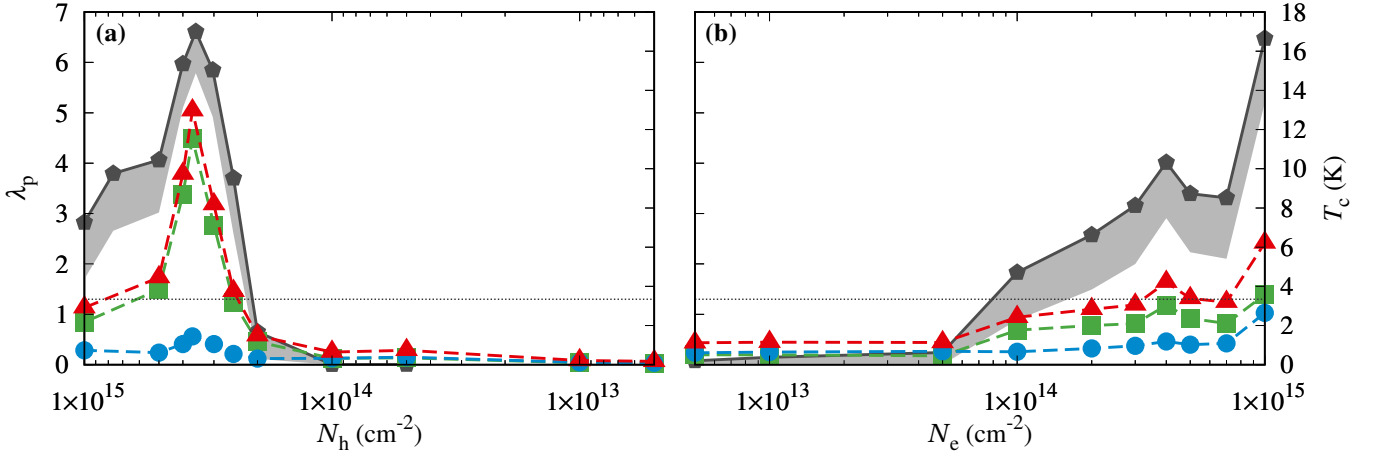


FIG. 4. Contributions to total electron-phonon coupling ( $\lambda_p$ ) and critical temperature ( $T_c$ ) as functions of hole (a) and electron (b) concentrations. Gray pentagons denote critical temperatures at  $\mu^* = 0.1$ . Gray shaded region represent variability of  $T_c$  with respect to  $\mu^*$ . Red triangles denote total electron phonon-coupling. Contributions to  $\lambda_p$  from acoustic and optical phonon modes are shown by green squares and blue circles, respectively. Dashed horizontal line corresponds to  $\lambda = 1.3$ .

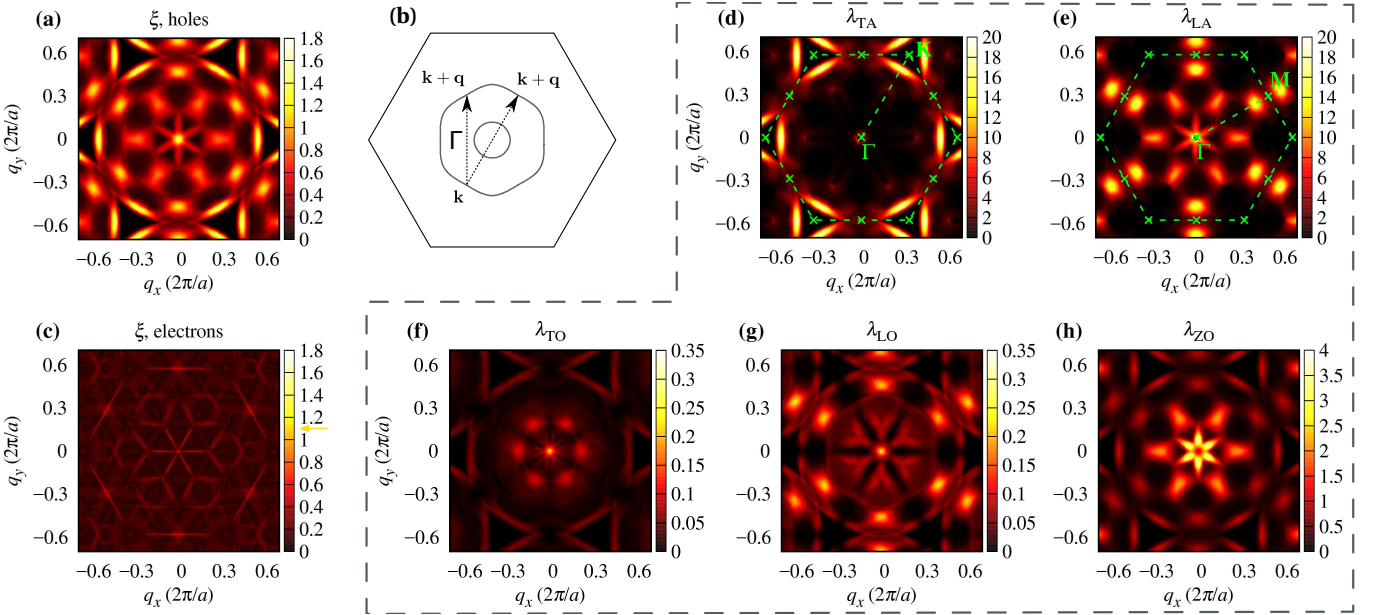


FIG. 5. Electron-phonon coupling and nesting function of doped antimonene. (a) and (c) show nesting function resolved in  $\mathbf{q}$ -space for  $N_h = 3.7 \times 10^{14} \text{ cm}^{-2}$  and  $N_e = 1 \times 10^{15} \text{ cm}^{-2}$ , respectively. Heatmaps are given on the same scale for clarity, whereas actual maximum of  $\xi$  is marked by a yellow arrow in (c). (b) shows the Fermi surface contour for  $N_h = 3.7 \times 10^{14} \text{ cm}^{-2}$ , where arrows mark two distinct electron scattering channels discussed in the text. In dashed frame (d)–(g) show electron-phonon coupling contributions from different phonon modes resolved in  $\mathbf{q}$ -space. Green labels in (c) and (d) mark the Brillouin zone and high symmetry directions.

is in general higher than that for other elemental monolayer materials discussed above. At comparable carrier concentrations,  $\lambda$  in the range of 0.5–1.4 was obtained for phosphorene [30], in the range of 0.76–1.27 for arsenene [31], while  $\lambda = 0.6$  was measured experimentally for Li-doped graphene at  $N_e = 1 \times 10^{14} \text{ cm}^{-2}$  [18]. Electron-phonon coupling strength of antimonene exceeds these values already at  $N_e = 1 \times 10^{14} \text{ cm}^{-2}$ . Despite significantly higher values of  $\lambda$ , this does not lead to a significant increase of  $T_c$  in comparison with the other

materials discussed. It can be explained by the difference in characteristic phonon frequencies for these systems (see Sec. III A), and particularly smaller values of  $\omega_{\log}$  [Eq. (7)]. As a result, in the context of superconductivity this effect compensates higher  $\lambda$ . The maximum value  $\lambda = 5$  is observed at  $N_h = 3.7 \times 10^{14} \text{ cm}^{-2}$ , indicating that hole-doped antimonene is a material with strong electron-phonon coupling. Electron-doped antimonene demonstrates considerably smaller  $\lambda$ , yet larger than in the other elemental 2D materials: at  $N_e > 3 \times 10^{14} \text{ cm}^{-2}$

one has  $\lambda > 1.3$ . We note that in the original work where Eq. (6) was derived [48], as well as in later works [70], it is pointed out that Eq. (6) underestimates  $T_c$  for materials with strong electron-phonon coupling, characterized by  $\lambda > 1.3$ . Therefore, the critical temperatures reported here should be considered as a lower limit.

As can be seen from Fig. 4, coupling with acoustic in-plane phonons (green squares) is the dominant contribution to  $\lambda$ . The coupling with optical phonons (blue circles) is small, but not negligible, at least in case of  $p$ -doping. We now consider  $\lambda_p$ , contributions from individual phonon modes to the electron-phonon coupling at  $N_h = 3.7 \times 10^{14} \text{ cm}^{-2}$ , which are presented in Fig. 5. The main contribution is provided by longitudinal acoustic mode with  $\lambda_{LA} = 2.7$ , while coupling with TA mode gives  $\lambda_{TA} = 1.8$ . As it was mentioned before, at  $N_h = 3.7 \times 10^{14} \text{ cm}^{-2}$  there is an indication of a strong Fermi surface nesting. To further investigate these phenomena, we calculate the nesting function  $\xi$  [Eq. (5)] shown in Fig. 5(a). Indeed,  $\xi$  exhibits maxima in the  $\Gamma$ -K direction of  $\mathbf{q}$ , corresponding to the momentum transfer between parallel sections of the Fermi surface [dotted line in Fig. 5(b)]. As can be seen from Fig. 5(d), this mechanism provides a dominant contribution to the coupling with TA phonons. At the same time, one can also see another set of peaks in  $\xi_{\mathbf{q}}$  along the  $\Gamma$ -M direction. These peaks correspond to the momentum transfer between non-parallel parts of the Fermi surface [dashed line in Fig. 5(b)]. This mechanism turns out to be more important for the coupling with LA phonons, which is shown in Fig. 5(e), resulting in a higher value of  $\lambda_{LA}$ . The electron-phonon coupling strengths for optical modes are two orders of magnitude smaller than those for the acoustic ones, with the exception of optical out-of-plane ZO mode [Figs. 5(f)-(h)].

Tabulated values of  $\lambda_p$  for different carrier concentrations are given in Supplemental Material (SM), Tables S1 and S2. As one can see,  $\lambda_{LA}$  remains the main contribution for other considered holes concentrations with the exception of  $N_h \leq 1 \times 10^{14} \text{ cm}^{-2}$ , as well as  $\lambda_{ZO}$  among optical phonon modes. For  $n$ -doping the situation is different. In this case the main contribution comes from the coupling with TA mode, while  $\lambda_{TO}$  is the highest contribution in the coupling with optical phonons. Similar to  $p$ -doping,  $\lambda_p$  of acoustic modes plays the major role. However, for  $N_e < 2 \times 10^{14} \text{ cm}^{-2}$  individual contributions of acoustic and optical phonons are of the same order. Distribution of the nesting function in  $\mathbf{q}$ -space for  $N_e = 1 \times 10^{15} \text{ cm}^{-2}$  is more complex [Fig. 5(b)] than for the hole doping [Fig. 5(a)]. This is because electron scattering now involves considerable intraband transitions. Therefore, it is not possible to determine specific scattering directions in this case. Here, the dominant contribution to  $\lambda$  arises from small  $\mathbf{q}$  (see SM, Fig. S1), contrary to a short-wavelength character of the electron-phonon coupling at  $N_h = 3.7 \times 10^{14} \text{ cm}^{-2}$ .

### C. Effects of bias voltage

The electronic bands of pristine antimonene are doubly degenerate with respect to spin [12], which is governed by the inversion symmetry. When an electric field is applied, the inversion symmetry is broken and the spin degeneracy is lifted, which gives rise to the band splitting. This can be clearly seen from Fig. 6, where we show the effect of bias voltage on the electronic structure of antimonene. Apart from the SOC related splitting, the band gap is enhanced by the field, unlike, for example, to few-layer phosphorene [41–43], where an opposite trend is observed. A small gap change of 0.1 eV is observed already at  $V_b = 1.0 \text{ V}$ , while the highest considered bias voltage of 1.6 V results in a gap of around 30% larger than the original one. DOS changes accordingly, as one can see from Fig. 6(a). Taking into account strong correlation of  $\lambda$  with DOS at the Fermi level, bias voltage is expected to have an effect on the superconducting critical temperatures. DOS at  $n$ - and  $p$ -doping behaves differently with the application of electric field. The most significant change of  $T_c$  is expected for  $p$ -doping at the concentrations corresponding to VHS at  $V_b = 0 \text{ V}$ . Due to the strong band splitting in the  $\Gamma$ -K direction, the flat band at  $\varepsilon_F \approx -1.3 \text{ eV}$  splits, resulting in two separate peaks in DOS. In contrast to the original VHS, the two resulting peaks have significantly smaller DOS, which becomes more clear at larger voltages. At the same time, DOS at lower carrier concentrations slowly increases with  $V_b$ , which is mostly observed for  $p$ -doping. The splitting of the VHS in the conduction band ( $n$ -doping) is less prominent.

Let us now consider how  $T_c$  depends on the carrier concentration in the presence of  $V_b = 1.0 \text{ V}$ . At this voltage one can clearly see qualitative changes of the carrier DOS [Fig. 6(a)], i.e. the splitting of a peak at  $\varepsilon_F \approx -1.3 \text{ eV}$ . As can be seen from Fig. 7(b), the change of  $T_c$  for the electron doping is nearly negligible at concentrations  $N_e < 3 \times 10^{14} \text{ cm}^{-2}$ . At higher concentrations,  $T_c$  increase of the order of 1.5 K is observed, with the exception of the highest considered concentration, which results in  $T_c$  being 1.5 K smaller than in  $V_b = 0 \text{ V}$  case. Maximum achievable  $T_c$  is now 14.6 K for high electron concentration  $9.4 \times 10^{14} \text{ cm}^{-2}$ , while hole doping gives comparable values of 13.4 and 12.1 K at  $N_h$  of  $2.7 \times 10^{14}$  and  $4.5 \times 10^{14} \text{ cm}^{-2}$ , respectively. This corresponds to two new local maxima in DOS. Interestingly,  $T_c$  at these points are in a good agreement with those observed at the same concentrations at  $V_b = 0 \text{ V}$ . High holes concentration of  $8.4 \times 10^{14} \text{ cm}^{-2}$  yields the critical temperature of 13 K, approximately 3 K higher than the highest considered concentration of  $1 \times 10^{15} \text{ cm}^{-2}$  in the absence of the bias voltage. Lower holes concentrations also yield higher  $T_c$  than in the absence of electric field:  $2 \times 10^{14} \text{ cm}^{-2}$  now gives  $T_c$  of 3.2 K, which is nearly twice as large as it was at  $V_b = 0 \text{ V}$ . While the absolute value of  $T_c$  enhancement at this concentration is small, it represents practically important trend: increase of the

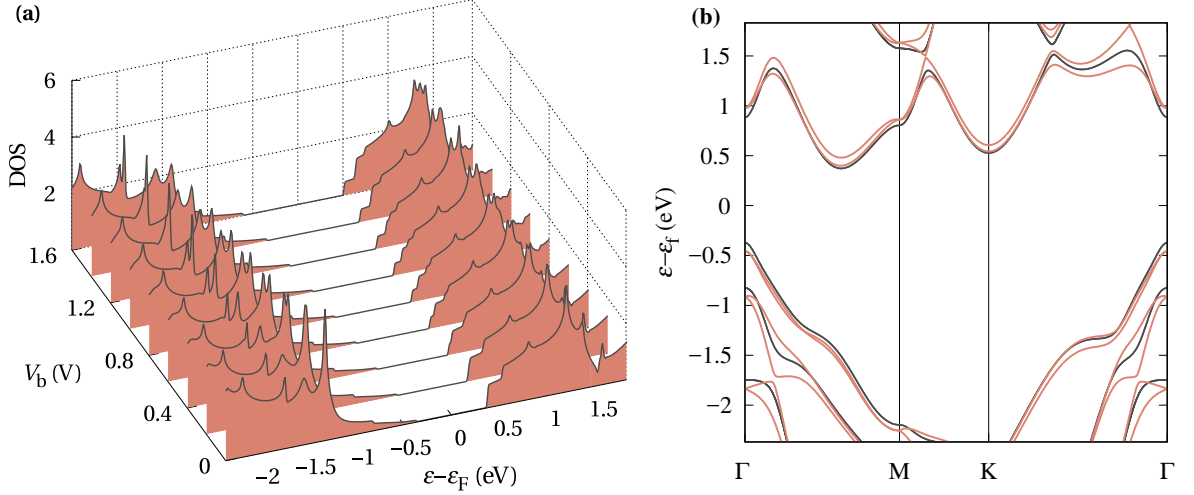


FIG. 6. Effect of applied bias voltage on the electronic structure of antimonene. (a) DOS at various values of bias voltage. (b) comparison of the electronic band structure for  $V_b=1.0$  V (red line) and  $V_b=0.0$  V (gray line).

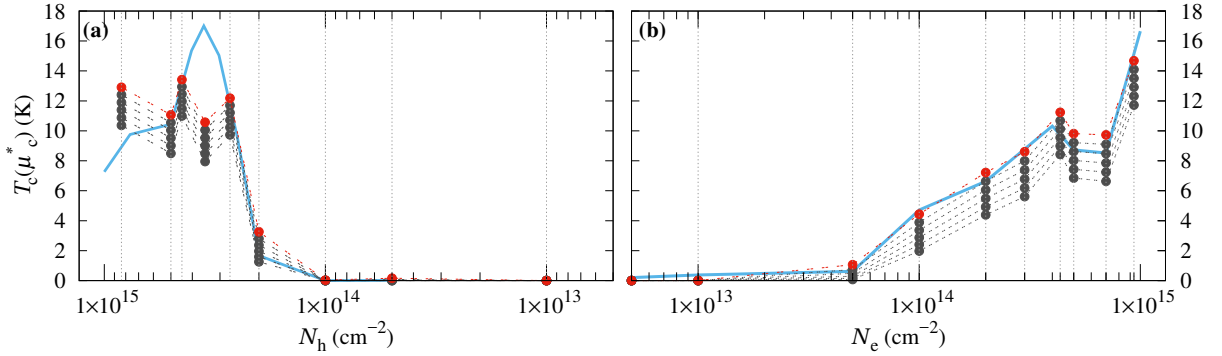


FIG. 7. Critical temperature dependence on carrier concentration at bias voltage of 1 V. Vertical lines mark relevant hole (a) and electron (b) concentrations. Six points for a single  $N_{h/e}$  represent different values of  $\mu_c^*$  (0.1, 0.12,...0.2). Blue solid line represents  $T_c$  at  $\mu_c^* = 0.1$  and  $V_b = 0.0$  V, and is given for comparison. Dashed lines serve as guide to the eye.

bias voltage allows to achieve higher values of  $T_c$  at lower concentrations.

We now turn to the dependencies of maximal critical temperature  $T_c^{\max}$  on the bias voltage [Fig. 8(a)] in the chosen carrier concentration range. As expected, the observed trends are different for different doping types. In the case of  $n$ -doping  $T_c^{\max}$  does not change significantly with bias, ranging from 14.6 K to 16.4 K with the lowest value corresponding to  $V_b = 0.4$  V. Concentrations required to achieve  $T_c^{\max}$  slowly decrease with bias voltage yet remaining high:  $N_e = 9 \times 10^{14} \text{ cm}^{-2}$  at  $V_b = 1.6$  V. As shown in Fig. 8(c), strong electron phonon coupling is observed for all considered concentrations with  $\lambda$  in the range of 2–3. At low bias voltages  $\lambda$  decreases first till  $V_b = 0.4$  V, and then increases in the rest of the range. The opposite trend is observed for  $p$ -doping. In this case,  $T_c^{\max}$  decreases monotonously with  $V_b$  from 17 to 10 K. The required hole concentration, on the contrary, increases, but not exceeding  $4.7 \times 10^{14} \text{ cm}^{-2}$ , which is still significantly smaller than for electrons. In the presence of bias voltage,  $\lambda$  reduces significantly from 5 to 1.8

yet indicating a sufficiently strong electron-phonon coupling.

Carrier concentrations presented in Fig. 8(b) are high, and thus may be difficult to achieve in practice. At the same time, bias voltage could increase DOS, as well as  $\lambda$  and  $T_c$  at moderate concentrations, i.e. below  $4 \times 10^{14} \text{ cm}^{-2}$ . In Figs. 8(d)-(e), we consider  $\lambda$  and  $T_c$  at more realistic concentrations of  $N_h = 2.5 \times 10^{14} \text{ cm}^{-2}$  and  $N_e = 3 \times 10^{14} \text{ cm}^{-2}$ , which are typical values in the medium concentration range. In case of electron doping, both  $\lambda$  and  $T_c$  increase monotonously with  $V_b$ , yet for the highest bias voltage considered,  $T_c$  increases by only  $\sim 1$  K. Hole doping yields  $\sim 2$  K enhancement of  $T_c$  already at  $V_b = 1.0$  V, while  $\lambda$  reaches the value of 2.0. In contrast to the case of electrons,  $\lambda$  and  $T_c$  exhibit a maximum at  $V_b \approx 1.2$  V, after which one can see a gradual decrease of their values. This behavior can be attributed to a decreasing DOS, shown in Fig. 6. Although in absolute values the effect of bias voltage is not large, it provides a possibility to increase  $T_c$  and  $\lambda$  in antimonene by up to 20%.



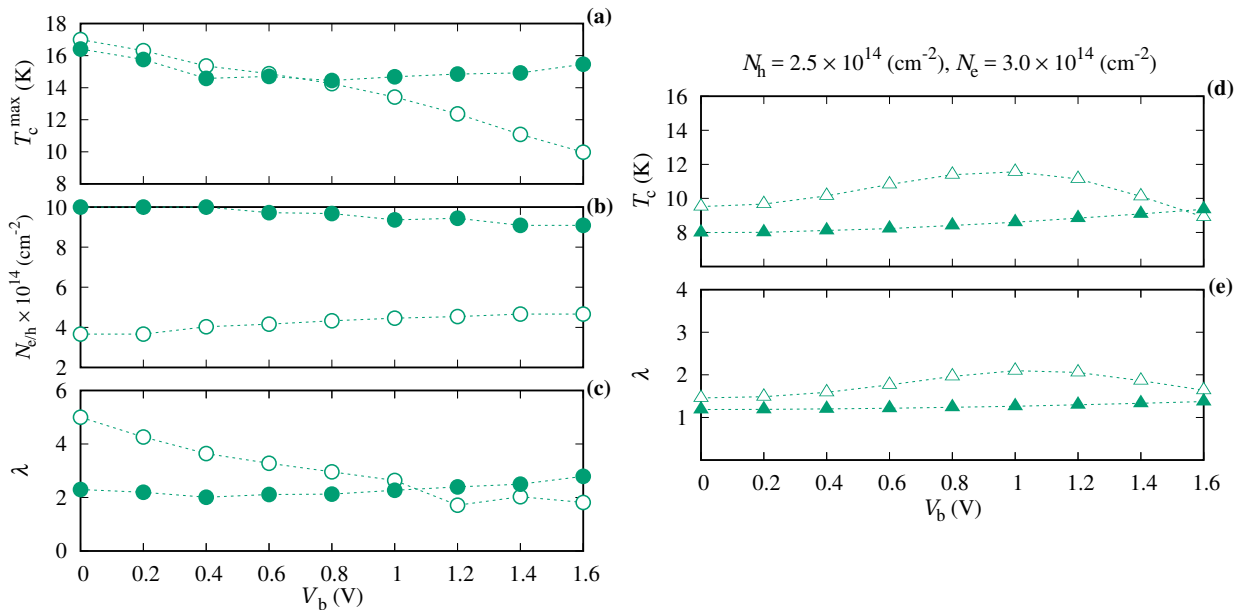


FIG. 8. Dependence of critical temperature and electron-phonon coupling in doped antimonene on the bias voltage. Filled and open symbols correspond to  $n$ - and  $p$ -doping cases: (a) maximal critical temperature  $T_c^{\max}$ ; (b) carrier concentration  $N_{e/h}$  corresponding to  $T_c^{\max}$ ; (c) total electron-phonon coupling strength  $\lambda$ . (d) and (e) show variation of critical temperature and electron-phonon coupling strength with bias voltage at fixed concentrations  $N_e = 3 \times 10^{14}$  cm $^{-2}$  (filled triangles) and  $N_h = 2.5 \times 10^{14}$  cm $^{-2}$  (open triangles).

#### IV. SUMMARY AND CONCLUSION

We performed *ab initio* calculations of electron-phonon coupling for  $n$ - and  $p$ -doped antimonene using state-of-the-art computational techniques. We estimated critical temperature of superconducting transition at various carrier concentrations in the wide range from  $5 \times 10^{13}$  to  $1 \times 10^{15}$  cm $^{-2}$  using Allen-Dynes-McMillan equation. Dependence of the electron-phonon coupling strength from carrier concentration is essentially conditioned by the doping type, and is mainly determined by the Fermi surface topologies. We find that at hole concentrations below  $2 \times 10^{14}$  cm $^{-2}$  and electron concentration below  $5 \times 10^{13}$  cm $^{-2}$  superconductivity is not expected above 0.5 K. Higher carrier concentrations yield  $T_c$  in a wide range, with the maximum values being 15 and 17 K for electron and hole doping, respectively. These values are comparable or exceed those reported for other doped elemental monolayer materials. At carrier concentration of  $3.7 \times 10^{14}$  cm $^{-2}$ , which corresponds to a van Hove singularity in the hole DOS, antimonene exhibits particularly strong electron-phonon coupling strength with  $\lambda = 5$ . This behavior can be attributed to the Fermi surface nesting, which is of interest on its own. For all studied carrier concentrations the main contribution to electron-phonon coupling arises from the interaction of carriers with in-plane acoustic phonons.

We also studied the effects of electric field applied in the direction perpendicular to the atomic sheet, on electron-phonon coupling and critical temperature of an-

timonene. In the bias voltage range of 0.0–1.6 V, the electronic structure of antimonene undergoes spin-orbit-assisted bands splitting, as well as enhancement of the band gap width. The effect is particularly noticeable in the  $p$ -doping case: spin splitting diminishes the VHS effects, leading to a reduction of maximum  $T_c$  by 7 K. At the same time critical temperature and electron-phonon coupling strength get slightly increased in the hole concentration range of  $1\text{--}3 \times 10^{14}$  cm $^{-2}$ . In contrast, electron doping case is less affected by the application of bias voltage, leading to a slight variation of the critical temperature and electron-phonon coupling over the whole concentration range. Overall, bias voltage allows to control electron-phonon coupling as well as related properties in heavy element 2D semiconductors, making them interesting objects for further studies.

#### V. ACKNOWLEDGMENTS

This work is part of the research programme “Two-dimensional semiconductor crystals” with project number 14TWOD01, which is (partly) financed by the Netherlands Organisation for Scientific Research (NWO). The calculations were performed at computational cluster “TCM”, Radboud University, Nijmegen, Netherlands and at computational cluster NUST “MISIS”, Moscow, Russia. A.N.R. acknowledges support from the Russian Science Foundation, Grant No. 17-72-20041.

- [1] S. Zhang, Z. Yan, Y. Li, Z. Chen, and H. Zeng, "Atomically Thin Arsenene and Antimonene: Semimetal-Semiconductor and Indirect-Direct Band-Gap Transitions," *Angew. Chem. Int. Ed.* **54**, 3112 (2015).
- [2] T. Lei, C. Liu, J.-L. Zhao, J.-M. Li, Y.-P. Li, J.-O. Wang, R. Wu, H.-J. Qian, H.-Q. Wang, and K. Ibrahim, "Electronic structure of antimonene grown on  $\text{Sb}_2\text{Te}_3$  (111) and  $\text{Bi}_2\text{Te}_3$  substrates," *J. Appl. Phys.* **119**, 015302 (2016).
- [3] P. Vogt, P. De Padova, C. Quaresima, J. Avila, E. Frantzeskakis, M. C. Asensio, A. Resta, B. Ealet, and G. Le Lay, "Silicene: Compelling Experimental Evidence for Graphenelike Two-Dimensional Silicon," *Phys. Rev. Lett.* **108**, 155501 (2012).
- [4] L. Zhang, P. Bampoulis, A. Rudenko, Q. Yao, A. van Houselt, B. Poelsema, M. Katsnelson, and H. Zandvliet, "Structural and Electronic Properties of Germanene on  $\text{MoS}_2$ ," *Phys. Rev. Lett.* **116**, 256804 (2016).
- [5] C. Gu, S. Zhao, J. L. Zhang, S. Sun, K. Yuan, Z. Hu, C. Han, Z. Ma, L. Wang, F. Huo, W. Huang, Z. Li, and W. Chen, "Growth of Quasi-Free-Standing Single-Layer Blue Phosphorus on Tellurium Monolayer Functionalized Au(111)," *ACS Nano* **11**, 4943 (2017).
- [6] P. Ares, J. J. Palacios, G. Abellán, J. Gómez-Herrero, and F. Zamora, "Recent Progress on Antimonene: A New Bidimensional Material," *Adv. Mater.* **30**, 1703771 (2018).
- [7] X. Wu, Y. Shao, H. Liu, Z. Feng, Y. L. Wang, J. T. Sun, C. Liu, J. O. Wang, Z. L. Liu, S. Y. Zhu, Y. Q. Wang, S. X. Du, Y. G. Shi, K. Ibrahim, and H. J. Gao, "Epitaxial Growth and Air-Stability of Monolayer Antimonene on  $\text{PdTe}_2$ ," *Adv. Mater.* **29**, 1605407 (2017).
- [8] C. Gibaja, D. Rodríguez-San-Miguel, P. Ares, J. Gómez-Herrero, M. Varela, R. Gillen, J. Maultzsch, F. Hauke, A. Hirsch, G. Abellán, and F. Zamora, "Few-Layer Antimonene by Liquid-Phase Exfoliation," *Angew. Chem. Int. Ed.* **55**, 14345 (2016).
- [9] P. Ares, F. Aguilar-Galindo, D. Rodríguez-San-Miguel, D. A. Aldave, S. Díaz-Tendero, M. Alcamí, F. Martín, J. Gómez-Herrero, and F. Zamora, "Mechanical Isolation of Highly Stable Antimonene under Ambient Conditions," *Adv. Mater.* **28**, 6332 (2016).
- [10] T. Morishita and M. J. Spencer, "How silicene on Ag(111) oxidizes: microscopic mechanism of the reaction of  $\text{O}_2$  with silicene," *Sci. Rep.* **5**, 17570 (2015).
- [11] S. Kuriakose, T. Ahmed, S. Balendhran, V. Bansal, S. Sriram, M. Bhaskaran, and S. Walia, "Black phosphorus: ambient degradation and strategies for protection," *2D Mater.* **5**, 032001 (2018).
- [12] A. N. Rudenko, M. I. Katsnelson, and R. Roldán, "Electronic properties of single-layer antimony: Tight-binding model, spin-orbit coupling, and the strength of effective Coulomb interactions," *Phys. Rev. B* **95**, 1 (2017).
- [13] G. Pizzi, M. Gibertini, E. Dib, N. Marzari, G. Iannaccone, and G. Fiori, "Performance of arsenene and antimonene double-gate MOSFETs from first principles," *Nat. Commun.* **7**, 12585 (2016).
- [14] D. Singh, S. K. Gupta, Y. Sonvane, and I. Lukačević, "Antimonene: a monolayer material for ultraviolet optical nanodevices," *J. Mater. Chem. C* **4**, 6386 (2016).
- [15] M. Zhao, X. Zhang, and L. Li, "Strain-driven band inversion and topological aspects in Antimonene," *Sci. Rep.* **5**, 16108 (2015).
- [16] T. Uchihashi, "Two-dimensional superconductors with atomic-scale thickness," *Supercond. Sci. Technol.* **30**, 013002 (2017).
- [17] M. M. Özer, J. R. Thompson, and H. H. Weitering, "Hard superconductivity of a soft metal in the quantum regime," *Nat. Phys.* **2**, 173 (2006).
- [18] B. M. Ludbrook, G. Levy, P. Nigge, M. Zonno, M. Schneider, D. J. Dvorak, C. N. Veenstra, S. Zhdanovich, D. Wong, P. Dosanjh, C. Straßer, A. Stöhr, S. Forti, C. R. Ast, U. Starke, and A. Damascelli, "Evidence for superconductivity in Li-decorated monolayer graphene," *Proc. Natl. Acad. Sci. U. S. A.* **112**, 11795 (2015).
- [19] Y. Ge, W. Wan, F. Yang, and Y. Yao, "The strain effect on superconductivity in phosphorene: a first-principles prediction," *New J. Phys.* **17**, 035008 (2015).
- [20] J. Chapman, Y. Su, C. A. Howard, D. Kundys, A. N. Grigorenko, F. Guinea, A. K. Geim, I. V. Grigorieva, and R. R. Nair, "Superconductivity in Ca-doped graphene laminates," *Sci. Rep.* **6**, 23254 (2016).
- [21] R. Zhang, J. Waters, A. K. Geim, and I. V. Grigorieva, "Intercalant-independent transition temperature in superconducting black phosphorus," *Nat. Commun.* **8**, 15036 (2017).
- [22] J. Lu, O. Zheliuk, Q. Chen, I. Leermakers, N. E. Hussey, U. Zeitler, and J. Ye, "Full superconducting dome of strong Ising protection in gated monolayer  $\text{WS}_2$ ," *Proc. Natl. Acad. Sci. U. S. A.* **115**, 3551 (2018).
- [23] X. Xi, Z. Wang, W. Zhao, J.-H. Park, K. T. Law, H. Berger, L. Forró, J. Shan, and K. F. Mak, "Ising pairing in superconducting  $\text{NbSe}_2$  atomic layers," *Nat. Phys.* **12**, 139 (2015).
- [24] J. M. Lu, O. Zheliuk, I. Leermakers, N. F. Q. Yuan, U. Zeitler, K. T. Law, and J. T. Ye, "Evidence for two-dimensional Ising superconductivity in gated  $\text{MoS}_2$ ," *Science* **350**, 1353 (2015).
- [25] J. T. Ye, Y. J. Zhang, R. Akashi, M. S. Bahramy, R. Arita, and Y. Iwasa, "Superconducting Dome in a Gate-Tuned Band Insulator," *Science* **338**, 1193 (2012).
- [26] Heersche Hubert B., Jarillo-Herrero Pablo, Oostinga Jeroen B., Vandersypen Lieven M. K., and Morpurgo Alberto F., "Bipolar supercurrent in graphene," *Nature* **446**, 56 (2007).
- [27] N. Yabuki, R. Moriya, M. Arai, Y. Sata, S. Morikawa, S. Masubuchi, and T. Machida, "Supercurrent in van der Waals Josephson junction," *Nat. Commun.* **7**, 10616 (2016).
- [28] G. Profeta, M. Calandra, and F. Mauri, "Phonon-mediated superconductivity in graphene by lithium deposition," *Nat. Phys.* **8**, 131 (2012).
- [29] E. R. Margine and F. Giustino, "Two-gap superconductivity in heavily n-doped graphene: Ab initio Migdal-Eliashberg theory," *Phys. Rev. B* **90**, 1 (2014).
- [30] D. F. Shao, W. J. Lu, H. Y. Lv, and Y. P. Sun, "Electron-doped phosphorene: A potential monolayer superconductor," *EPL* **108**, 67004 (2014).
- [31] X. Kong, M. Gao, X.-W. Yan, Z.-Y. Lu, and T. Xiang, "Superconductivity in electron-doped arsenene," (2018), [arXiv:1801.00545](https://arxiv.org/abs/1801.00545).

- [32] A. P. Durajski, D. Szczśniak, and R. Szczśniak, “Study of the superconducting phase in silicene under biaxial tensile strain,” *Solid State Commun.* **200**, 17 (2014).
- [33] Y. Ge and A. Y. Liu, “Phonon-mediated superconductivity in electron-doped single-layer MoS<sub>2</sub>: A first-principles prediction,” *Phys. Rev. B* **87**, 241408 (2013).
- [34] P. Hohenberg and W. Kohn, “Inhomogeneous Electron Gas,” *Phys. Rev.* **136**, B864 (1964).
- [35] W. Kohn and L. J. Sham, “Self-Consistent Equations Including Exchange and Correlation Effects,” *Phys. Rev.* **140**, A1133 (1965).
- [36] X. Gonze and C. Lee, “Dynamical matrices, Born effective charges, dielectric permittivity tensors, and interatomic force constants from density-functional perturbation theory,” *Phys. Rev. B* **55**, 10355 (1997).
- [37] F. Giustino, M. L. Cohen, and S. G. Louie, “Electron-phonon interaction using Wannier functions,” *Phys. Rev. B* **76**, 165108 (2007).
- [38] N. Marzari, A. A. Mostofi, J. R. Yates, I. Souza, and D. Vanderbilt, “Maximally localized Wannier functions: Theory and applications,” *Rev. Mod. Phys.* **84**, 1419 (2012).
- [39] Z. Ni, Q. Liu, K. Tang, J. Zheng, J. Zhou, R. Qin, Z. Gao, D. Yu, and J. Lu, “Tunable Bandgap in Silicene and Germanene,” *Nano Lett.* **12**, 113 (2012).
- [40] A. Acun, L. Zhang, P. Bampoulis, M. Farmanbar, A. van Houselt, A. N. Rudenko, M. Lingenfelder, G. Brocks, B. Poelsema, M. I. Katsnelson, and H. J. W. Zandvliet, “Germanene: the germanium analogue of graphene,” *J. Phys. Condens. Matter* **27**, 443002 (2015).
- [41] A. N. Rudenko, S. Yuan, and M. I. Katsnelson, “Toward a realistic description of multilayer black phosphorus: From *GW* approximation to large-scale tight-binding simulations,” *Phys. Rev. B* **92**, 085419 (2015).
- [42] J. Kim, S. S. Baik, S. H. Ryu, Y. Sohn, S. Park, B.-G. Park, J. Denlinger, Y. Yi, H. J. Choi, and K. S. Kim, “Observation of tunable band gap and anisotropic dirac semimetal state in black phosphorus,” *Science* **349**, 723 (2015).
- [43] Q. Liu, X. Zhang, L. B. Abdalla, A. Fazzio, and A. Zunger, “Switching a Normal Insulator into a Topological Insulator via Electric Field with Application to Phosphorene,” *Nano Lett.* **15**, 1222 (2015).
- [44] A. Kormányos, V. Zólyomi, N. D. Drummond, P. Rakyta, G. Burkard, and V. I. Fal’ko, “Monolayer MoS<sub>2</sub>: Trigonal warping, the  $\Gamma$  valley, and spin-orbit coupling effects,” *Phys. Rev. B* **88**, 045416 (2013).
- [45] F. Giustino, “Electron-phonon interactions from first principles,” *Rev. Mod. Phys.* **89**, 015003 (2017).
- [46] T. Bazhiron, J. Noffsinger, and M. L. Cohen, “Superconductivity and electron-phonon coupling in lithium at high pressures,” *Phys. Rev. B* **82**, 184509 (2010).
- [47] W. L. McMillan, “Transition Temperature of Strongly-Coupled Superconductors,” *Phys. Rev.* **167**, 331 (1968).
- [48] P. B. Allen and R. C. Dynes, “Transition temperature of strong-coupled superconductors reanalyzed,” *Phys. Rev. B* **12**, 905 (1975).
- [49] A. B. Migdal, “Interactions between electrons and lattice vibrations in a normal metal,” *Sov. Phys. JETP* **34**, 1438 (1958).
- [50] G. M. Eliashberg, “Interactions between electrons and lattice vibrations in a superconductor,” *Sov. Phys. JETP* **11**, 966 (1960).
- [51] P. Morel and P. W. Anderson, “Calculation of the Superconducting State Parameters with Retarded Electron-Phonon Interaction,” *Phys. Rev.* **125**, 1263 (1962).
- [52] L. Peters, A. N. Rudenko, and M. I. Katsnelson, “*Ab initio* study of the electron-phonon coupling at the Cr(001) surface,” *Phys. Rev. B* **97**, 165438 (2018).
- [53] P. Giannozzi, S. Baroni, N. Bonini, M. Calandra, R. Car, C. Cavazzoni, D. Ceresoli, G. L. Chiarotti, M. Cococcioni, I. Dabo, A. D. Corso, S. Fabris, G. Fratesi, S. de Gironcoli, R. Gebauer, U. Gerstmann, C. Gougousis, A. Kokalj, M. Lazzeri, L. Martin-Samos, N. Marzari, F. Mauri, R. Mazzarello, S. Paolini, A. Pasquarello, L. Paulatto, C. Sbraccia, S. Scandolo, G. Sclauzero, A. P. Seitsonen, A. Smogunov, P. Umari, and R. M. Wentzcovitch, “QUANTUM ESPRESSO: a modular and open-source software project for quantum simulations of materials,” *J. Phys. Condens. Matter* **21**, 395502 (2009).
- [54] P. Giannozzi, O. Andreussi, T. Brumme, O. Bunau, M. Buongiorno Nardelli, M. Calandra, R. Car, C. Cavazzoni, D. Ceresoli, M. Cococcioni, N. Colonna, I. Carnimeo, A. Dal Corso, S. de Gironcoli, P. Delugas, R. A. DiStasio, A. Ferretti, A. Floris, G. Fratesi, G. Fugallo, R. Gebauer, U. Gerstmann, F. Giustino, T. Gorni, J. Jia, M. Kawamura, H.-Y. Ko, A. Kokalj, E. Küçükbenli, M. Lazzeri, M. Marsili, N. Marzari, F. Mauri, N. L. Nguyen, H.-V. Nguyen, A. Otero-de-la Roza, L. Paulatto, S. Poncé, D. Rocca, R. Sabatini, B. Santra, M. Schlipf, A. P. Seitsonen, A. Smogunov, I. Timrov, T. Thonhauser, P. Umari, N. Vast, X. Wu, and S. Baroni, “Advanced capabilities for materials modelling with Quantum ESPRESSO,” *J. Phys. Condens. Matter* **29**, 465901 (2017).
- [55] H. J. Monkhorst and J. D. Pack, “Special points for Brillouin-zone integrations,” *Phys. Rev. B* **13**, 5188 (1976).
- [56] S. Poncé, E. R. Margine, C. Verdi, and F. Giustino, “EPW: Electronphonon coupling, transport and superconducting properties using maximally localized Wannier functions,” *Comput. Phys. Commun.* **209**, 116 (2016).
- [57] T. Sohler, M. Calandra, and F. Mauri, “Density functional perturbation theory for gated two-dimensional heterostructures: Theoretical developments and application to flexural phonons in graphene,” *Phys. Rev. B* **96**, 75448 (2017).
- [58] D. Daghero, F. Paolucci, A. Sola, M. Tortello, G. A. Ummarino, M. Agosto, R. S. Gonnelli, J. R. Nair, and C. Gerbaldi, “Large Conductance Modulation of Gold Thin Films by Huge Charge Injection via Electrochemical Gating,” *Phys. Rev. Lett.* **108**, 66807 (2012).
- [59] D. K. Efetov and P. Kim, “Controlling Electron-Phonon Interactions in Graphene at Ultrahigh Carrier Densities,” *Phys. Rev. Lett.* **105**, 256805 (2010).
- [60] K. Xu, H. Lu, E. W. Kinder, A. Seabaugh, and S. K. Fullerton-Shirey, “Monolayer Solid-State Electrolyte for Electric Double Layer Gating of Graphene Field-Effect Transistors,” *ACS Nano* **11**, 5453 (2017).
- [61] G. Wang, R. Pandey, and S. P. Karna, “Atomically thin group V elemental films: Theoretical investigations of antimonene allotropes,” *ACS Appl. Mater. Interfaces* **7**, 11490 (2015).
- [62] M. I. Katsnelson, I. I. Naumov, and A. V. Trefilov, “Singularities of the electronic structure and pre-martensitic anomalies of lattice properties in  $\beta$ -phases of metals and alloys,” *Phase Transit.* **49**, 143 (1994).

- [63] A. Landa, P. Söderlind, I. Naumov, J. Klepeis, and L. Vitos, “Kohn Anomaly and Phase Stability in Group VB Transition Metals,” [Computation](#) **6**, 29 (2018).
- [64] S. Wang, W. Wang, and G. Zhao, “Thermal transport properties of antimonene: an ab initio study,” [Phys. Chem. Chem. Phys.](#) **18**, 31217 (2016).
- [65] D. Liu, A. G. Every, and D. Tománek, “Continuum approach for long-wavelength acoustic phonons in quasi-two-dimensional structures,” [Phys. Rev. B](#) **94**, 165432 (2016).
- [66] Z. Zhu and D. Tománek, “Semiconducting layered blue phosphorus: A computational study,” [Phys. Rev. Lett.](#) **112**, 1 (2014), 1403.1300.
- [67] A. N. Rudenko, S. Brener, and M. I. Katsnelson, “Intrinsic Charge Carrier Mobility in Single-Layer Black Phosphorus,” [Phys. Rev. Lett.](#) **116**, 246401 (2016).
- [68] M. I. Katsnelson, “Flexuron: A self-trapped state of electron in crystalline membranes,” [Phys. Rev. B](#) **82**, 205433 (2010).
- [69] J. Zhao, M. Wang, X. Zhang, Y. Lv, T. Wu, S. Qiao, S. Song, and B. Gao, “Application of sodium-ion-based solid electrolyte in electrostatic tuning of carrier density in graphene,” [Sci. Rep.](#) **7**, 3168 (2017).
- [70] V. Z. Kresin, “On the critical temperature for any strength of the electron-phonon coupling,” [Phys. Lett. A](#) **122**, 434 (1987).